Supporting Information

In vivo imaging of axonal transport of mitochondria in the diseased and aged mammalian CNS

Yuji Takihara, Masaru Inatani, Kei Eto, Toshihiro Inoue, Alexander Kreymerman, Seiji Miyake, Shinji Ueno, Masatoshi Nagaya, Ayami Nakanishi, Keiichiro Iwao, Yoshihiro Takamura, Hirotaka Sakamoto, Keita Satoh, Mineo Kondo, Tatsuya Sakamoto, Jeffrey L. Goldberg, Junichi Nabekura, and Hidenobu Tanihara

Contents:

Note: Movies S1–S15 are available on the PNAS website.

SI Methods

Animals. We obtained *Thy1-mitoCFP* mice (1) from the Jackson Laboratory. Each line expresses diverse patterns of CFP in the nervous system. We chose *Thy1-mitoCFP-S* mice for this study after confirming that the CFP expression pattern in RGCs was the most suitable for MIMIR. In all experiments, heterozygous *Thy1-mitoCFP-S* mice were used. We defined the age of mice as follows: young, 2 months; adult, 4 months; middle-aged, 12–13 months; and old, 23–25 months.

Immunogold Labeling. *Thy1-mitoCFP-S* mice were anesthetized and transcardially perfused with phosphate-buffered saline (PBS), followed by 4% paraformaldehyde and 0.1% glutaraldehyde in 0.1 M phosphate buffer (PB). After the eyes with optic nerves were quickly excised and the anterior segment, lens, and vitreous body were removed, the eyecups were immersed in 4% paraformaldehyde in 0.1 M PB for 3 h at room temperature. The samples were dehydrated in a methanol series and embedded in LR Gold resin (Electron Microscopy Sciences) and polymerized under UV lamps at −20°C for 24 h. Ultrathin midsagittal sections (70 nm in thickness) through ONH were collected on grids and treated with 1% normal goat serum and 2% bovine serum albumin in PBS for 30 min. The sections were then incubated with a 1:20 dilution of rabbit monoclonal antibody to green fluorescent protein (GFP) (Cell Signaling Technology, 2956) for 2 h at 30°C. After washing with PBS, the sections were incubated with a 1:50 dilution of a goat anti-rabbit IgG-gold conjugate F(ab′)$_2$ fragment (particle diameter, 10 nm) for 1 h at room temperature (BBI Solutions, EM.GFAR10). They were electron-stained with uranyl acetate and lead citrate. Images were obtained with an electron microscope (Hitachi, H-7650).

Explant Imaging of the Retina Using a Multiphoton Microscope. The retinal explants of *Thy1-mitoCFP-S* mice were obtained and maintained under the condition optimized for long-term retinal cultures as described previously (2) with minor modification. Immediately after the mice were euthanized, the optic nerves were cut and the eyes were excised and immersed in Hanks' Balanced Salt Solution with penicillin (100 units/mL) and streptomycin (100 μg/mL) on ice. After the anterior segment, lens, and vitreous body were removed, the retina was peeled from the sclera. The whole retina with four radial cuts was flat-mounted using sterilized mesh (SEFAR) and tape (Thermo Scientific), with the RGC side down on a 35-mm glass-bottom dish (MatTek). Then, for explant imaging using an upright microscope, the 35-mm dish was gently turned over and placed in a 60-mm dish filled with culture medium consisting of Neurobasal-A medium (Life Technologies) supplemented with 2% B-27 supplement (Life Technologies), 1% N-2 supplement (Life Technologies), 0.8 mM L-glutamine (Sigma-Aldrich), 100 units/mL penicillin, and 100 μg/mL streptomycin (Life Technologies), avoiding air bubbles in the 35-mm dish. Explant imaging of the retina was conducted using a multiphoton upright microscope (Carl Zeiss, LSM 710 NLO) equipped with a chamber kept at 35°C and 5% CO$_2$ (Tokai Hit) (2). The central retina near ONH was imaged using the laser tuned at 860 nm from a mode-locked Ti: sapphire laser (Coherent, Chameleon Vision II) and a 20× water-immersion objective with a numerical aperture of 1.0 and a working distance of 1.8 mm (Carl

Zeiss). Using a pixel dwell time of 2.55 µs, retinal images with a field of view of 128.6 × 128.6 µm (512 × 512 pixels) were acquired every 3 s for 3 min with no averaging.

MIMIR Using a Multiphoton Microscope. To generate an incipient congenic albino line of the *Thy1-mitoCFP-S* mice, the *Thy1-mitoCFP-S* mice were backcrossed to BALB/c mice for at least five generations and maintained (3). The mice were anesthetized with intraperitoneal injection of 120 mg/kg ketamine and 18 mg/kg xylazine. The depth of anesthesia was assessed by monitoring the toe pinch reflex. We placed an anesthetized mouse on a heating pad with monitoring to maintain the body temperature at 36–37°C. After the temporal skin of the eye (asterisk in Fig. S3*A*) was opened, the conjunctiva (the area surrounded by arrows in Fig. S3*A*) was opened for MIMIR, resulting in almost no bleeding. Custom-made metal bars were attached to the skull to reduce the artifacts caused by heartbeat and breathing (Fig. S3*B*). We put a 24 × 36-mm coverslip (Matsunami Glass) on the exposed sclera (Fig. S3*B*) to make a flat plane in front of a 25× water-immersion objective with a numerical aperture of 1.05 and a working distance of 2.0 mm (Olympus).

The laser pulses tuned at 860 nm (< 15 mW at the sample) from a mode-locked Ti: sapphire laser (Spectra Physics, MaiTai DeepSee) on a multiphoton laser-scanning upright microscope (Olympus, Fluoview FV1000MPE) were focused on the peripheral retina through the sclera using the 25× objective. Fluorescence was collected by the 25× objective and directed to a dichroic mirror (NRDM690), an interference filter (32BA685RIF), and an external non-descanned photomultiplier tube. Using a pixel dwell time of 4.0 µs, retinal images with a field of view of 126.7 × 126.7 µm (512 × 512 pixels) were acquired every 3 s for 3 min with no averaging for quantification of mitochondrial axonal transport. In order to create a completely dark environment for the highly sensitive photomultiplier tubes, we conducted MIMIR using shade curtains to cover all parts of the multiphoton microscope and turned off all the lights in the imaging room.

Quantification of Mitochondrial Axonal Transport in Vivo. We analyzed images using MetaMorph software (Molecular Devices) and the indicated modules. Kymographs were generated using Stack Arithmetic (maximum) and by drawing a region of interest. In kymographs, diagonal lines represent mitochondrial movement, whereas vertical lines represent stationary mitochondria and/or varicosities. We defined mitochondrial axonal transport as mitochondrial movement with a velocity of ≥ 0.05 µm/s. Diagonal lines of velocity < 0.05 µm/s were regarded as pauses. Duty cycle was calculated as the percentage of time spent in transport. Velocity of mitochondrial axonal transport was calculated as the distance of transport without pauses divided by the duration of transport. Mitochondria-free regions in axons were measured using the kymograph from the first to the second plane by the Integrated Morphometry Analysis function. We defined the length of mitochondria as the length parallel to the axonal long axis. We analyzed only one segment per axon for quantification of mitochondrial axonal transport.

Immunohistochemistry for GFAP. Mice were anesthetized as previously described and received either MIMIR or optic nerve crush. Four hours post imaging or 72 h post crush, the animals were anesthetized and perfused with the fixative 4% paraformaldehyde–PBS. Scleral areas where MIMIR took place were marked with trypan blue. The eyes were excised, followed by removal of the cornea and lens. A suture was placed around the imaged area of the retina, which allowed identification of the imaged areas vs. the non-imaged areas on sections. Then the eyes were fixed for an additional 4 h, transferred to a 30% sucrose–PBS solution, and stored at 4°C overnight, prior to OCT embedding for cryo-sectioning. The eyes were cryo-sectioned at 10 μm thickness, and permeabilized for 1 h in a blocking solution (0.2% Triton X-100, 150 mM NaCl, 50 mM Tris base, 1% bovine serum albumin, 100 mM L-lysine, 0.04% azide, and 5% neonatal goat serum, pH 7.4). The sections were incubated with GFAP antibody (Abcam, ab7260, diluted to 1:500 in blocking solution) at 4°C overnight. The sections were washed three times with PBS and incubated with Alexa Fluor® 546 goat anti-rabbit (Life Technologies, A-11035) in a blocking solution at room temperature for 2 h. The sections were washed and mounted in ProLong® Gold with DAPI (Life Technologies, P-36931). All slides were imaged using an Olympus FluoView1000 confocal system.

Intravitreal Injection of *N*-Methyl-D-Aspartate. Intravitreal injection was performed using a method described previously (4) with minor modifications. In brief, the mice were anesthetized, and the pupil was dilated using a solution of 0.5% tropicamide and 0.5% phenylephrine (Santen Pharmaceutical, Mydrin-P). Next, a topical anesthetic (Santen Pharmaceutical, Benoxil solution 0.4%) was administered before intravitreal injection of 1 μl of a 30 nmol *N*-methyl-D-aspartate solution (Sigma-Aldrich) to induce RGC apoptosis (5). The solution was injected 1 mm from the temporal corneal limbus using a 32-gauge needle attached to a micro syringe (Ito Corporation).

Annexin V Labeling. Annexin V conjugated with Alexa Fluor 594 (Life Technologies) was diluted with PBS in a 1:1 ratio. Four hours after MIMIR or 24 h after *N*-methyl-D-aspartate injection, the mice were anesthetized and 1 μL of diluted Annexin V was injected into the vitreous from the nasal limbus side. One hour after Annexin V injection, the mice were anesthetized and transcardially perfused with 4% paraformaldehyde in PBS; then, the eye was enucleated. The retina was flat-mounted on a slide glass (Matsunami Glass) and mounted using ProLong® Gold antifade reagent (Life Technologies) and a coverslip (Matsunami Glass). Because of nonspecific staining in the retina around the Annexin V injection site as described previously (5), we acquired images from the hemiretina opposite to the side where Annexin V was injected. The images were acquired using a confocal laser scanning microscope (Carl Zeiss, LSM 710 NLO) with a 20× objective.

OHT and Intraocular Pressure Measurements. *Thy1-mitoCFP-S* mice were anesthetized by intraperitoneal injection of 100 mg/kg ketamine and 9 mg/kg xylazine. After the mice lost consciousness and failed to blink after topical instillation of saline, they were placed on the stage in front of a slit lamp microscope with a diode laser (NIDEK, GYC-1500; 532 nm). To obstruct the

aqueous humor, photocoagulation of limbal and episcleral veins (150 mW laser power, 0.2 s, 100 μm diameter) was performed unilaterally. Photocoagulation (250 mW laser power, 0.2 s, 50 μm diameter) was conducted for deeper episcleral veins. We performed photocoagulation of the limbal vein over 300°, avoiding the long posterior ciliary arteries. Antibiotic ointment was administered after laser treatment. To measure intraocular pressure, after setting a rebound tonometer (Icare Finland Oy, TonoLab), the mice were anesthetized by intraperitoneal injection of 100 mg/kg ketamine and 9 mg/kg xylazine. Intraocular pressure measurements were performed from 4 min to 7 min after intraperitoneal injection when intraocular pressure did not appreciably change under the anesthesia.

Evaluation of RGC Axon Degeneration in the OHT Group. To evaluate the degeneration of RGC axons in the OHT group, paraphenylenediamine staining and axon counts in optic nerves were conducted as described previously, with some modifications (6). Paraphenylenediamine darkly stains the axoplasm of degenerated axons. The optic nerves were fixed with 0.8% paraformaldehyde and 1.2% glutaraldehyde in 0.1 M PB (pH 7.4) overnight at 4°C and then incubated in 2% osmium tetroxide in 0.1 M PB for 5 h at 4°C. After washing three times in 0.1 M PB for 10 min, the optic nerves were dehydrated in a graded ethanol series and placed in propylene oxide. They were then incubated in a mixture of propylene oxide and Epok 812 (Oken) and embedded with Epok 812. Sections (thickness, 1 μm) were cut and stained with 1% paraphenylenediamine in isopropanol/methanol (1:1) for 28 min. We obtained images first using a 20× objective (Olympus, BX51 microscope) to evaluate the optic nerve cross-sectional areas and then a 100× objective to count axons. After opening all the images using Photoshop software (Adobe Systems), we placed a 20 × 15 μm box on the topmost image. We used the software to excise the same boxed area in all the images, which included images invisible to the operator. Intact axons were counted using ImageJ (United States National Institutes of Health).

Immunohistochemistry for CFP and Brn-3. We used the antibody (MBL, 598; 1:2,000) to GFP to detect CFP expressed in mitochondria. Retinal whole mounts were fixed in 4% paraformaldehyde and were incubated in 0.4% Triton X-100 in PBS for 90 min at room temperature. The whole mounts were blocked in 0.5% bovine serum albumin in PBS overnight at 4°C for the antibody to GFP or 10% normal donkey serum in PBS with 0.1% Triton X-100 (PBST) for 1 h at room temperature for the antibody to Brn-3. The rabbit polyclonal antibody to GFP or the goat polyclonal antibody to Brn-3 (Santa Cruz Biotechnology, sc-6026; 1:50) was applied at 4°C for 24 h (anti-GFP) or overnight (anti-Brn-3). After three washes in PBS (anti-GFP) or PBST (anti-Brn-3), the whole mounts were incubated with anti-rabbit secondary antibody conjugated with Alexa 488 (Life Technologies; 1:2,000) or anti-goat secondary antibody conjugated with Alexa 594 (Life Technologies; 1:1,000) overnight at 4°C. The whole mounts with four radial cuts were mounted in ProLong® Gold Antifade Reagent (Life Technologies). We acquired images using a confocal laser scanning microscope (Olympus, Fluoview 500) with a 20× objective at central (250 μm from ONH), middle (800 μm from ONH), and peripheral

(100 μm from the ora serrata) locations in each area of the retina between radial cuts. Brn-3-positive RGC nuclei in 12 images per retina were counted with ImageJ and averaged.

Laser Microdissection of the Retina. To obtain total RNA of RGCs from the mouse retina, we used laser microdissection technique to eliminate the inner nuclear, outer plexiform, and outer nuclear layers. Optic nerve crush in mice was performed as described previously (7) with minor modifications. *Thy1-mitoCFP-S* mice (4 months) were anesthetized by intraperitoneal injection of 100 mg/kg ketamine and 9 mg/kg xylazine. The optic nerve (1 mm from the eyeball) was exposed and crushed using self-crossing forceps for 10 s. After performing fundus examination of the mice to check for normal blood circulation in the retina, we applied an antibiotic ointment to the eye. After the mice were euthanized, the eyes were enucleated and immediately frozen in Tissue-Tek OCT compound (Sakura Finetek Japan). Serial cryosections (thickness, 20 μm) were cut and mounted on dry heat-sterilized FrameSlides (PET-Membrane 1.4 μm) (Leica Biosystems). All mounted sections were fixed in ethanol/acetic acid (19:1) for 3 min and then washed once with diethylpyrocarbonate-treated water (DEPC water) for 1 min. Following staining of nuclei with 0.05% toluidine blue in DEPC water for 1 min, the sections were washed twice with DEPC water for 1 min and then air-dried. The specimens were stored at −80°C until use. The FrameSlides were mounted on a Leica AS LMD system (Leica Biosystems). The nerve fiber, ganglion cell, and inner plexiform layers dissected by laser were collected into the cap of a microcentrifuge tube, which was filled with buffer RLT (RNeasy Mini Kit, Qiagen, Hilden, Germany) placed underneath the section. After laser microdissection, the cap was closed and the contents were centrifuged to collect films at the bottom of the microcentrifuge tube.

RNA Extraction and Real-Time RT-PCR. Total RNA was isolated using the RNeasy Micro Kit (Qiagen) according to the manufacturer's instruction. The concentration of total RNA was quantified using NanoDrop 2000c (Thermo Fisher Scientific) and the quality was analyzed using Agilent 2100 Bioanalyzer (Agilent Technologies). In our condition, all RNA samples were used as the template for reverse transcription because not only did each RNA integrity number value exceed 5 (8), but there was also no significant difference between the RNA integrity number value of the control samples (5.5 ± 0.54) and optic nerve crush samples (5.8 ± 0.83).

Complementary DNA was synthesized from total RNA as the template using ReverTra Ace® qPCR RT Kit (TOYOBO) according to the manufacturer's instruction. Real-time RT-PCR was performed using THUNDERBIRD® SYBR® qPCR Mix (TOYOBO) and StepOnePlus Real-Time PCR system (Life Technologies) with the following thermal profile: 95°C for 1 min, followed by 40 cycles of 95°C for 3 s and 60°C for 60 s. The primers were as follows: PGC-1α (forward 5′-GATGAATACCGCAAAGAGCA-3′ and reverse 5′-AGATTTACGGTGCATTCCTCA-3′), NRF-1 (forward 5′-GGTACAGGGGCAACAGTAGC-3′ and reverse 5′-CGTGGCCCAGTTTTGTTC-3′), and β-actin (forward 5′-AGGCATTGCTGACAGGATG-3′ and reverse 5′-ACAGAGTACTTGCGCTCAGGA-3′). The mRNA levels were evaluated by the ΔΔCT method and normalized to β-actin mRNA levels.

Electroretinogram. The techniques for recording the electroretinograms from mice have been described in detail previously (9). In brief, the mice were dark-adapted overnight and then anesthetized with intraperitoneal injection of 70 mg/kg ketamine and 14 mg/kg xylazine. Electroretinograms were recorded using a gold-wire loop electrode placed on the cornea and a reference electrode on the sclera. The mice were placed in a Ganzfeld bowl and stimulated with stroboscopic stimuli of 1.0 log cd-s/m^2 (photopic units) maximum intensity. Four levels of stimulus intensities ranging from −5.0 to 1.0 log cd-s/m^2 were used for scotopic electroretinogram recordings, and four levels of stimulus intensities ranging from −0.5 to 1.0 log cd-s/m^2 were used for photopic electroretinogram recordings. The photopic electroretinograms were recorded on a rod-suppressing white background of 1.3 log cd-s/m^2.

Statistical Analysis. We analyzed the results of mitochondrial axonal transport in five mice (one eye per mouse) under each condition (Figs. 2–4). We used the Shapiro–Wilk test to assess normality and Levene's test to assess the equality of variances. When normality was indicated, Student's or Welch's *t*-test was used. When normality was questioned, the Mann–Whitney test was used. For comparisons of intraocular pressure between the control and OHT groups at each time point (Fig. S7*A*) and amplitude of electroretinograms at different levels of stimulus intensities (Fig. S9), Bonferroni correction was used. For multiple comparisons, one-way analysis of variance with post hoc Tukey's honestly significant difference test (Fig. S7 *E* and *I*) or the Kruskal–Wallis test with post hoc Dunn's test (Figs. 3 and S10) was used. All results are shown as mean ± SEM. $P < 0.05$ was considered statistically significant using the JMP statistical package (SAS Institute).

SI Text

Reduction in Mitochondrial Axonal Transport in the Glaucoma Model. Increased energy demand in RGCs caused by elevated intraocular pressure may be associated with the reduction in the number of transported mitochondria in the glaucoma model. Impaired mitochondrial axonal transport has been shown in studies of other neurodegenerative models (10–12). In glaucoma, elevated intraocular pressure is suggested to induce RGC axon injury and reduction in axonal transport resulting in RGC death (13–16). Elevated intraocular pressure in primate eyes results in accumulation of mitochondria in RGC axons (17). However, to date, investigations of mitochondrial axonal transport in glaucoma have been limited to histological observations. In the glaucoma model in the present study, compression of RGC axons at the lamina in ONH (6) may contribute to the reduction in mitochondrial axonal transport in vivo. Axonal injury decreases ATP levels in the damaged axons of rat dorsal root ganglion neurons (18). Elevated intraocular pressure decreases ATP levels in the optic nerves of DBA/2J mice (19). Together with these data, our results suggest that increased energy demand in RGCs caused by elevated intraocular pressure is associated with the reduction in mitochondrial axonal transport.

Imbalance Between Mitochondrial Fusion/Fission in the Glaucoma Model and with Aging. An imbalance between mitochondrial fusion/fission is suggested to be involved in many

neurodegenerative diseases. In mammals, dynamin-related protein 1 (Drp1) and fission 1 (Fis1) mainly participate in the mitochondrial fission process, whereas optic atrophy 1 (OPA1) and mitofusin 1 and 2 (Mfn1 and 2) are mainly involved in the mitochondrial fusion process. We believe that the reduced length of mitochondria transported in RGC axons of the glaucoma model results from increased mitochondrial fission and/or reduced mitochondrial fusion, because excessive mitochondrial fragmentation was observed (Fig. S2 and Movie S1) in the retinal explants after cutting of the optic nerves (RGC axons). Moreover, a histological study of RGC axons of DBA/2J mice showed mitochondrial fission (20). In the brains of patients with Alzheimer's disease, there is an increase in the levels of S-nitrosylation of Drp1, which is suggested to have high fission activity by enhanced dimerization (21). Mutations in OPA1 cause autosomal dominant optic atrophy, a degenerative disease of RGCs (22, 23). Mutations in Mfn2 are associated with Charcot–Marie–Tooth disease type 2A (24).

Previous studies have suggested that an imbalance between mitochondrial fusion/fission may be involved in the aging process. However, with aging, it remains controversial which imbalance (mitochondrial fragmentation or enlargement) between mitochondrial fusion/fission mainly occurs. The data regarding increased Fis1 levels in aged rats relative to young rats (25) favor our results regarding the reduced length of mitochondria transported in axons in aged mice. However, an increase in *Drosophila* Mfn levels in aged flies compared with young flies has been reported (26).
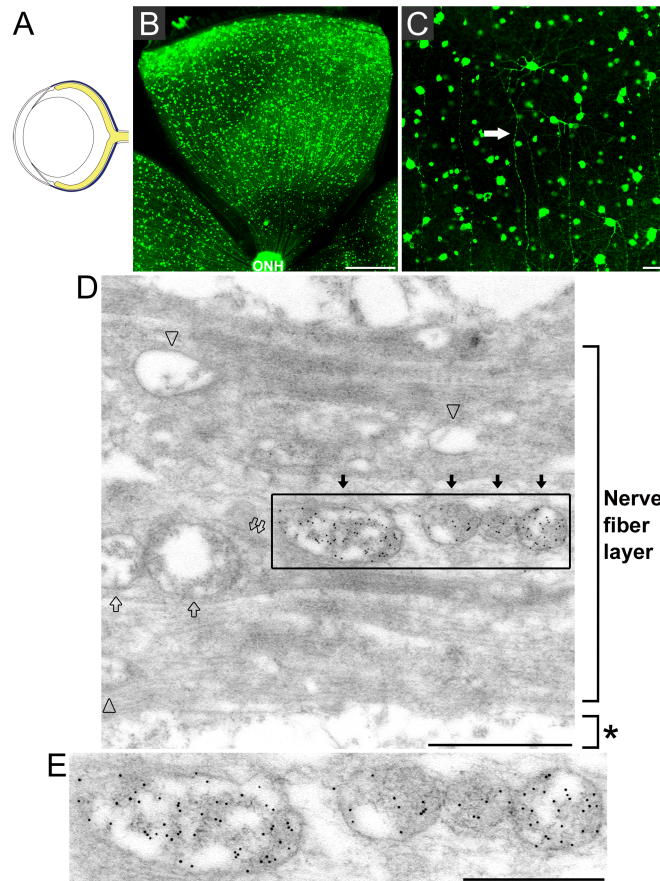
Fig. S1. CFP is specifically expressed in mitochondria sparsely enough to identify individual RGC axons in *Thy1-mitoCFP-S* mice. (*A*) Schematic of the mouse eye (yellow, retina and optic nerves; blue, sclera). (*B*) Immunohistochemical analysis of a retinal whole mount of *Thy1-mitoCFP-S* mice shows RGC axons that projected to ONH. (Scale bar, 500 µm.) (*C*) Magnification of *B* indicated that the RGC axon (arrow) is distinct because CFP is sparsely expressed in the *Thy1-mitoCFP-S* retina. (Scale bar, 50 µm.) (*D* and *E*) Immunogold labeling of the nerve fiber layer of the retina indicated that CFP is specifically expressed in mitochondria in part of RGC axons in *Thy1-mitoCFP-S* mice. (*D*) An RGC cell body (asterisk) is present on the lower side of *D*. RGC axons in the nerve fiber layer are extended in the horizontal direction in *D*. All mitochondria (arrows) in an axon were labeled by multiple 10-nm gold particles. Mitochondria (open arrows) in another axon (double open arrows) next to the axon that contained specifically labeled mitochondria (arrows) were not labeled by gold particles nor were mitochondria (open arrowheads) in the other axons in *D*. (Scale bar, 1 µm.) (*E*) Higher magnification of the boxed area in *D* confirmed that CFP is specifically expressed in mitochondria. (Scale bar, 0.5 µm.)
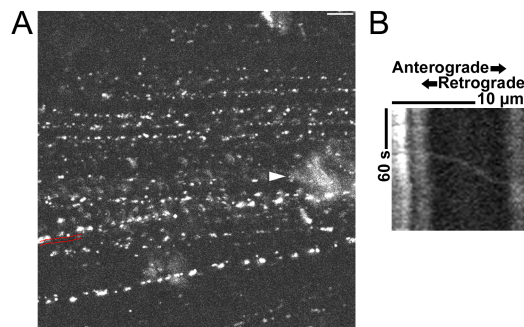
Fig. S2. Explant imaging of the retina of *Thy1-mitoCFP-S* mice using a multiphoton microscope shows mitochondrial axonal transport in RGC axons. (*A*) Representative image of explant imaging of the retina of *Thy1-mitoCFP-S* mice (arrowhead, RGC cell body), showing one mitochondrial axonal transport (Movie S1). Note that explant imaging was conducted at the central retina near ONH where the density of RGC axons is high because mitochondrial axonal transport in the retinal explants was rarely observed although the retinal explants were obtained and maintained under the conditions optimized for long-term retinal cultures. Cutting of the optic nerves (RGC axons) to prepare the retinal explants induced excessive mitochondrial fragmentation in RGC axons. (Scale bar, 10 μm.) (*B*) A kymograph (a representation of mitochondrial positions in an axon during the recording time) of the axon indicated by red parallel lines in *A* detected one mitochondrial axonal transport, shown as a diagonal line. ONH is on the right side of *A*.
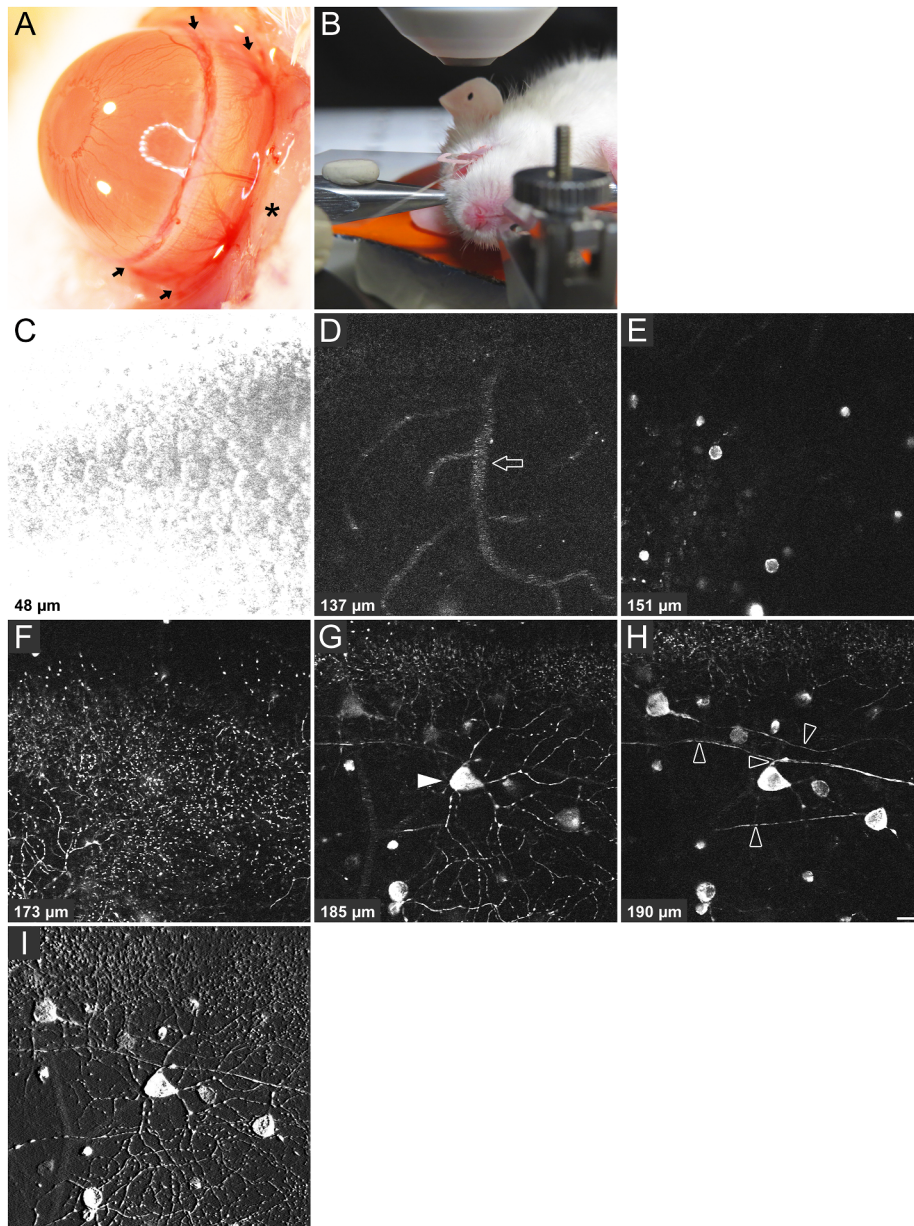
Fig. S3. *Z*-stack images of minimally invasive intravital imaging of the mouse retina through the sclera show individual RGC axons. (*A*) Minimally invasive opening of the skin (asterisk) and conjunctiva (the area surrounded by arrows) in an albino line of *Thy1-mitoCFP-S* mice considerably improves the accessibility (i.e., minimal absorption and scattering of light) of the mouse retina, making this accessibility similar to that of the zebrafish CNS for intravital imaging. (*B*) Minimally invasive intravital imaging of the mouse retina through the sclera. To make a flat plane in front of a water-immersion objective, a coverslip was placed on the exposed sclera. (*C*–*H*) *Z*-stack images of minimally invasive intravital imaging of the mouse retina through the sclera (the area surrounded by arrows in *A*) using a multiphoton microscope (Movie S2) reveal distinct layers in the retina, including the retinal pigment epithelium (*C*), deeper layer of the retinal vascular system (*D*, open arrow), inner nuclear layer (*E*), inner plexiform layer (*F*), RGC cell bodies and dendrites (*G*, arrowhead) in the ganglion cell layer, and individual RGC axons in the nerve fiber layer (*H*, open arrowheads). Individual RGC axons commonly project to ONH in *H*. (Scale bar, 20 μm.) (*I*) Three-dimensional images (Movie S3) from the inner plexiform layer to the nerve fiber layer reveal a whole image of RGC (arrowhead in *G*) at subcellular resolution, which includes the RGC axon and dendrites. ONH is on the right side of *C*–*I*. Depth is indicated at the lower left of *C*–*H*.
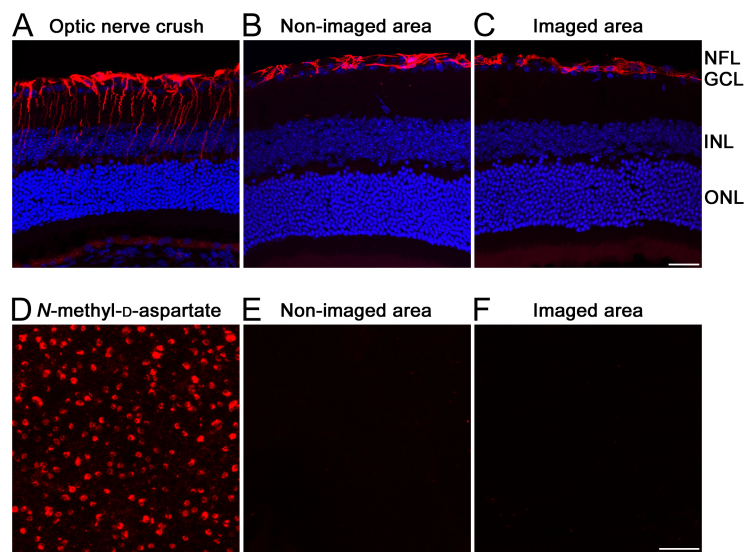
Fig. S4. MIMIR does not induce glial-based inflammatory responses in the retina or RGC apoptosis. (*A*) Representative image of astrocytes/Müller glia inflammatory responses in the retina after optic nerve crush. GFAP, a marker of glial inflammation, was strongly upregulated by cells in the nerve fiber layer (NFL) and ganglion cell layer (GCL), with additional GFAP-filled projections into the inner nuclear (INL) and outer nuclear layers (ONL), identified by DAPI staining (blue) and GFAP (red) immunoreactivity. (*B*) Non-imaged area of the retina in a MIMIR imaged eye, showing typical GFAP expression in the NFL and GCL, with no immunoreactivity in the INL or ONL compared with *A*. (*C*) MIMIR imaged area of the retina, showing no sign of increased GFAP immunoreactivity compared with *B*. (Scale bar, 30 μm.) (*D*) Representative image of apoptotic cells in the retina after intravitreal injection of *N*-methyl-D-aspartate (30 nmol). Apoptotic cells labeled with Annexin V conjugated with Alexa Fluor 594 (red) in the GCL. (*E*) Non-imaged area of the retina in a MIMIR imaged eye, showing no Annexin V-positive RGCs. (*F*) MIMIR imaged area of the retina, showing no Annexin V-positive RGCs. (Scale bar, 50 μm.)
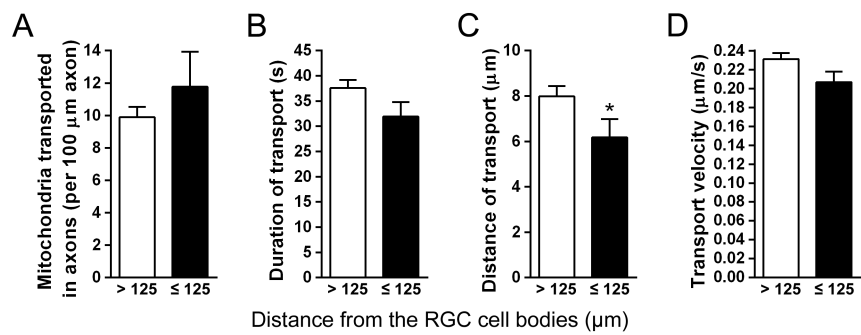
Fig. S5. MIMIR shows that in axons whose distance from the soma is ≤ 125 μm, the distance of mitochondrial transport is shorter than that in the axons > 125 μm from the soma. (*A–D*) In the axons ≤ 125 μm from the soma, the duration (*B*) and distance (*C*, *$P = 0.01$) of mitochondrial transport were shorter than those in the axons > 125 μm from the soma. The Mann–Whitney test (two-tailed) was used for calculation of *P* values in *A–D*. The results are shown as mean ± SEM. The sample size (*n*) for each group is given in Table S2.
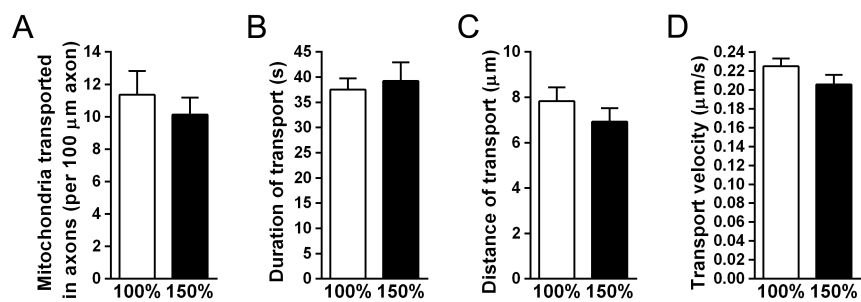
Fig. S6. Different excitation intensity did not change the mitochondrial dynamics, suggesting that CFP emission by MIMIR does not affect the mitochondrial dynamics. (*A–D*) The number of mitochondria transported in axons (*A*) and the duration (*B*), distance (*C*), and velocity (*D*) of mitochondrial axonal transport imaged by 150% MIMIR standard excitation intensity were not significantly different compared with those imaged by MIMIR standard excitation intensity (100%). The Mann–Whitney test (two-tailed) was used for calculation of *P* values in *A–D*. The results are shown as mean ± SEM. The sample size (*n*) for each group is given in Table S2.
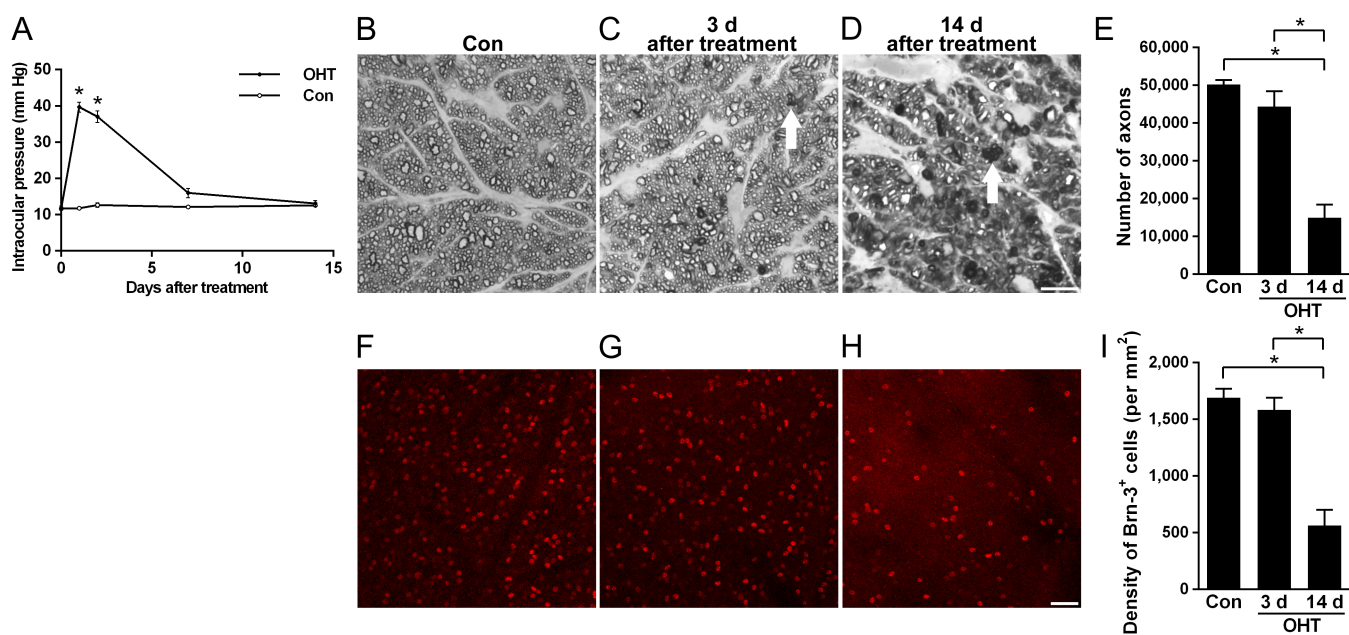
Fig. S7. OHT induces glaucomatous changes in mouse RGCs. (*A*) Laser treatment induced elevated intraocular pressure (*$P < 0.0001$) 1 and 2 d after treatment. Intraocular pressure in the OHT group declined and returned to the control (Con) level in 2 weeks. (*B–D*) Cross-sections of optic nerves stained by paraphenylenediamine are shown for control (*B*), 3 d after laser treatment (*C*), and 14 d after laser treatment (*D*). Paraphenylenediamine darkly stained the axoplasm of degenerating axons (arrows). (Scale bar, 10 μm.) (*E*) OHT induced significant axon degeneration in optic nerves 14 d after laser treatment (*$P < 0.0001$). (*F–H*) Immunohistochemistry with the antibody to Brn-3 (an RGC marker) of a retinal whole mount is shown for control (*F*), 3 d after laser treatment (*G*), and 14 d after laser treatment (*H*). (Scale bar, 50 μm.) (*I*) OHT induced significant RGC death 14 d after laser treatment (*$P < 0.0001$). The results are shown as mean ± SEM. Control, $n = 15$ eyes; OHT, $n = 15$ eyes in *A*; control, $n = 6$ eyes; and OHT, $n = 6$ eyes in *E* and *I*.
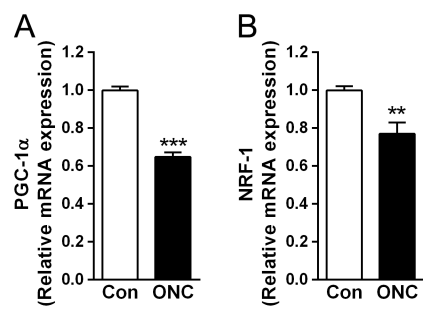
Fig. S8. mRNA expression of a key transcriptional coactivator (PGC-1α) and transcription factor (NRF-1) of mitochondrial biogenesis decreases 3 d after RGC axon injury compared with that in control (Con) retinas. (*A* and *B*) mRNA expression of PGC-1α (*A*, ****P* < 0.001) and NRF-1 (*B*, ***P* < 0.01) was measured using real-time RT-PCR of samples obtained by laser microdissection of control retinas and optic nerve crush (ONC) retinas 3 d after treatment. The expression of PGC-1α and NRF-1 was normalized to β-actin mRNA expression. Student's *t*-test (two-tailed) was used for calculation of *P* values in *A* and *B*. The results are shown as mean ± SEM of 6 eyes in each group.
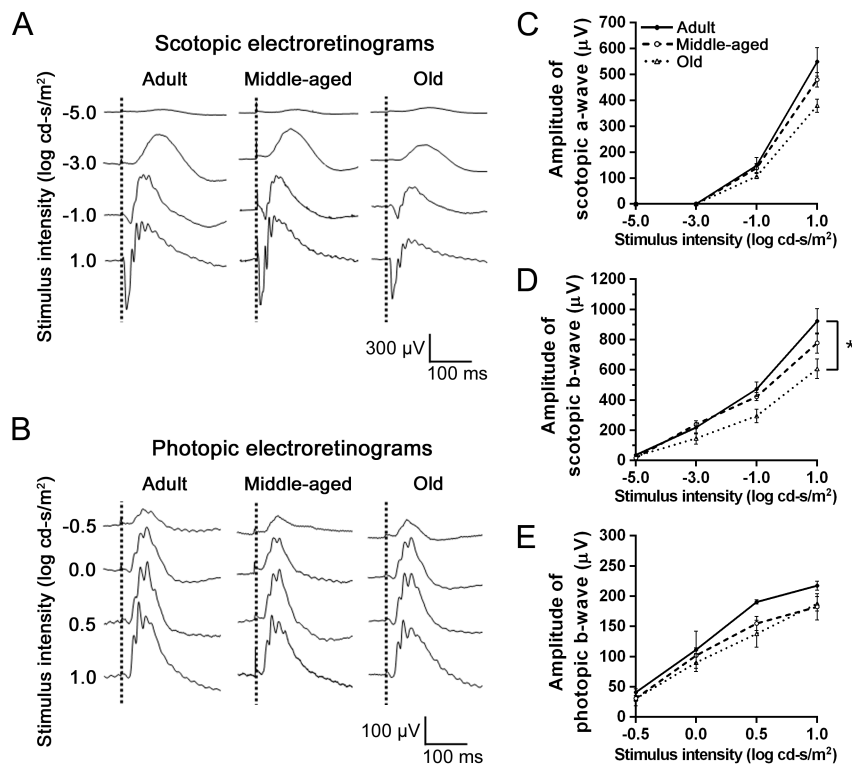
Fig. S9. Amplitude of electroretinograms from old mice decreases compared with that from adult mice. (*A* and *B*) Representative scotopic (*A*) and photopic (*B*) electroretinograms elicited by four different stimulus intensities from adult, middle-aged, and old mice. (*C*) Amplitude of scotopic a-wave from adult, middle-aged, and old mice. (*D*) Amplitude of scotopic b-wave from adult, middle-aged, and old mice. The amplitude of scotopic b-wave elicited by 1.0 log cd-s/m² from old mice significantly decreased (**P* < 0.05) compared with that from adult mice. (*E*) Amplitude of photopic b-wave from adult, middle-aged, and old mice. Student's *t*-test with Bonferroni correction (two-tailed) was used for calculation of *P* values in *C–E*. The results are shown as mean ± SEM. Adult, *n* = 4; middle-aged, *n* = 4; and old, *n* = 4 in *C–E*.
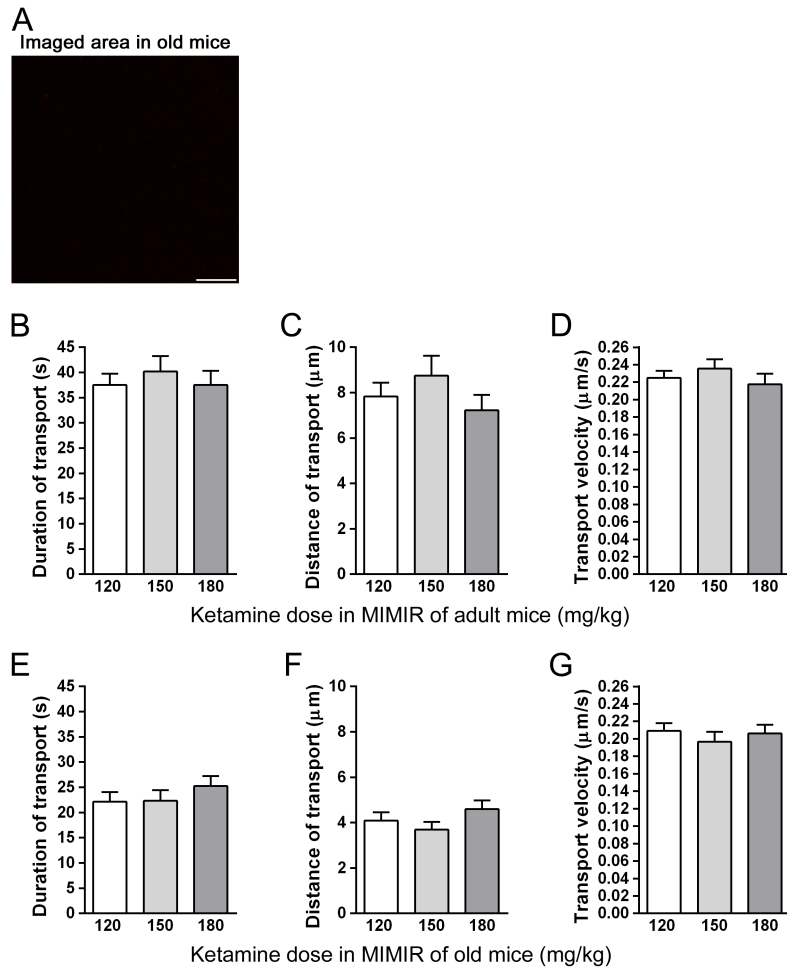
Fig. S10. No significant ketamine dose-dependent effects on the dynamics of mitochondrial axonal transport in adult or old mice were observed, suggesting that shorter mitochondrial transport in old mice than that in adult mice does not result from different depths of anesthesia between adult and old mice in MIMIR. (*A*) No Annexin V-positive RGCs were observed in the MIMIR imaged area of the retina of old mice, suggesting that the ketamine dose (120 mg/kg) intraperitoneally injected in the standard MIMIR procedure did not induce RGC apoptosis in old mice. (Scale bar, 50 μm.) (*B*–*G*) No significant ketamine dose-dependent effects (120–180 mg/kg) on the dynamics of mitochondrial axonal transport in adult (*B*–*D*) or old (*E*–*G*) mice were observed. The Kruskal–Wallis test was used for calculation of *P* values in *B*–*G*. The results are shown as mean ± SEM. The sample size (*n*) for each group is given in Table S2.
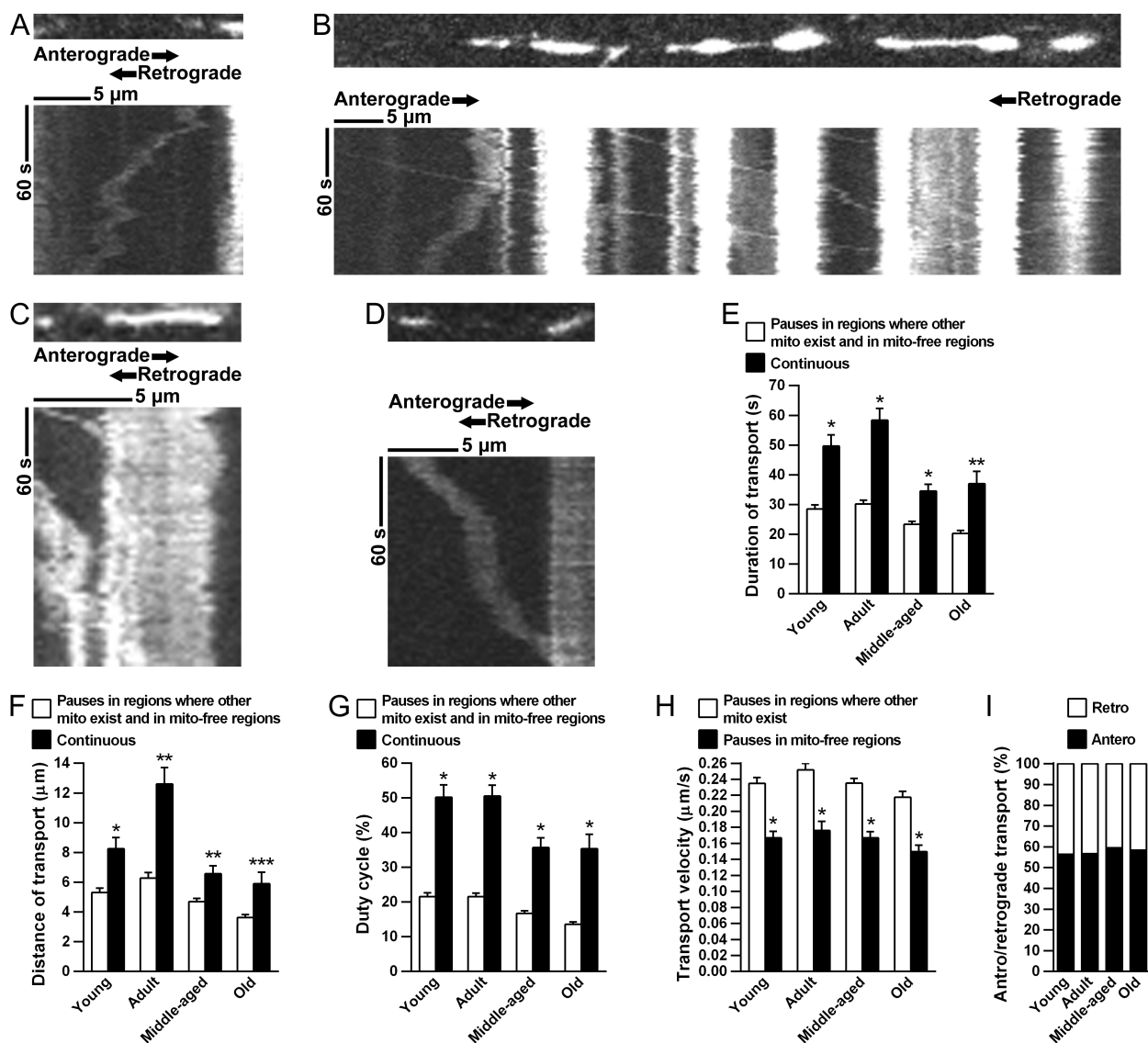
Fig. S11. MIMIR suggests total organization of mitochondrial transport preserved in mice aged up to 23–25 months. (*A–D*) Representative images of four transport patterns: bilateral transport (*A*, Movie S11); continuous transport (*B*, Movie S12); transport that pauses in regions where other mitochondria exist (*C*, Movie S13); and transport that pauses in mitochondria-free regions (*D*, Movie S14). (*E–G*) Continuous transport had the longest duration (*E*, *$P < 0.0001$, **$P = 0.0002$) and distance (*F*, *$P = 0.0003$, **$P < 0.0001$, ***$P = 0.03$) of uninterrupted transport and duty cycle (*G*, *$P < 0.0001$). (*H*) The velocity of transport that pauses in mitochondria-free regions was slower than that of transport that pauses in regions where other mitochondria exist (*$P < 0.0001$). (*I*) The consistent ratios of anterograde/retrograde transport (approximately 3:2 ratio) among the four age groups support total organization of mitochondrial axonal transport preserved in mice aged up to 23–25 months. The Mann–Whitney test (two-tailed) was used in *E–H* for comparison between two groups in each age group. The results are shown as mean ± SEM. The sample size (*n*) for each group is given in Tables S1 and S2.

A

Mitochondria-free region in axons (%)

Adult Old
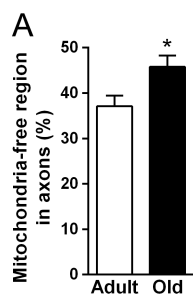
Fig. S12. RGC axons in old mice, compared with those in adult mice, have a vulnerability to stresses resulting from an increase in the mitochondria-free regions in axons. (*A*) The mitochondria-free regions increased in RGC axons of old mice (*$P = 0.03$) compared with those of adult mice. In axons, the increase in mitochondria-free regions indicates an increase in regions inadequately supported by mitochondria. The Mann–Whitney test (two-tailed) was used for calculation of *P* value in *A*. The results are shown as mean ± SEM. The sample size (*n*) for each group is given in Table S2.

Table S1. The sample size (*n*) for each group in Figures 2–4 and S11*I*

Figure	Group	*n*
Fig. 2 *E–G* and *L*	Control	78 axons
	OHT	70 axons
Fig. 2 *H*, *I*, and *K*	Control	608 transport
	OHT	322 transport
Fig. 2*J*	Control	512 mitochondria
	OHT	268 mitochondria
Fig. 2*M*	Control	512 mitochondria
	OHT	282 mitochondria
Fig. 3 *E–G* and *L*	Young	68 axons
	Adult	78 axons
	Middle-aged	85 axons
	Old	70 axons
Fig. 3 *H*, *I*, *K*, and *N* Fig. S11*I*	Young	581 transport
	Adult	608 transport
	Middle-aged	684 transport
	Old	413 transport
Fig. 3*J*	Young	477 mitochondria
	Adult	512 mitochondria
	Middle-aged	597 mitochondria
	Old	362 mitochondria
Fig. 3*M*	Young	453 mitochondria
	Adult	512 mitochondria
	Middle-aged	579 mitochondria
	Old	343 mitochondria
Fig. 4 *B–D*	Adult	70 axons
	Old	47 axons

Table S2. The sample size (*n*) for each group in Figures S5, S6, and S10–S12

Figure	Group		*n*
Fig. S5*A*	> 125 µm		65 axons
	≤ 125 µm		13 axons
Fig. S5 *B–D*	> 125 µm		489 transport
	≤ 125 µm		119 transport
Fig. S6*A*	100%		26 axons
	150%		16 axons
Fig. S6 *B–D*	100%		257 transport
	150%		109 transport
Fig. S10 *B–D*	120 mg/kg		257 transport
	150 mg/kg		184 transport
	180 mg/kg		122 transport
Fig. S10 *E–G*	120 mg/kg		146 transport
	150 mg/kg		144 transport
	180 mg/kg		153 transport
Fig. S11 *E* and *F*	Young	Transport pauses	423 transport
		Continuous	142 transport
	Adult	Transport pauses	429 transport
		Continuous	149 transport
	Middle-aged	Transport pauses	516 transport
		Continuous	149 transport
	Old	Transport pauses	332 transport
		Continuous	68 transport
Fig. S11*G*	Young	Transport pauses	359 mitochondria
		Continuous	110 mitochondria
	Adult	Transport pauses	364 mitochondria
		Continuous	127 mitochondria
	Middle-aged	Transport pauses	453 mitochondria
		Continuous	129 mitochondria
	Old	Transport pauses	295 mitochondria
		Continuous	58 mitochondria
Fig. S11*H*	Young	Pauses in regions where other mito exist	305 transport
		Pauses in mito-free regions	118 transport
	Adult	Pauses in regions where other mito exist	317 transport
		Pauses in mito-free regions	112 transport
	Middle-aged	Pauses in regions where other mito exist	413 transport
		Pauses in mito-free regions	103 transport
	Old	Pauses in regions where other mito exist	265 transport
		Pauses in mito-free regions	67 transport
Fig. S12*A*	Adult		78 axons
	Old		70 axons

Titles of Movies S1–S15

Movie S1. Explant imaging of the retina of *Thy1-mitoCFP-S* mice.

Movie S2. Z-stack images of minimally invasive intravital imaging of the mouse retina through the sclera.

Movie S3. Three-dimensional images of minimally invasive intravital imaging of the mouse retina from the inner plexiform layer to the nerve fiber layer.

Movie S4. MIMIR shows highly dynamic mitochondrial axonal transport in vivo under physiological conditions.

Movie S5. MIMIR shows mitochondria transported from and to the RGC cell body.

Movie S6. MIMIR shows characteristically long, snake-like mitochondria transported in an axon.

Movie S7. MIMIR of adult control mice (age, 4 months).

Movie S8. MIMIR of adult mice with experimental glaucoma 3 d after laser treatment.

Movie S9. MIMIR of middle-aged mice (age, 12–13 months).

Movie S10. MIMIR of old mice (age, 23–25 months).

Movie S11. MIMIR shows bilateral mitochondrial axonal transport.

Movie S12. MIMIR shows continuous mitochondrial axonal transport.

Movie S13. MIMIR shows that mitochondrial axonal transport pauses in the region where other mitochondria exist.

Movie S14. MIMIR shows that mitochondrial axonal transport pauses in the mitochondria-free region.

Movie S15. MIMIR of old mice with experimental glaucoma 3 d after laser treatment.

SI Movie Legends

Movie S1. Explant imaging of the retina (arrowhead, RGC cell body) of *Thy1-mitoCFP-S* mice shows mitochondrial axonal transport in an RGC axon (asterisk). ONH is on the right side of Movie S1. Note that this explant imaging was conducted near ONH where the density of RGC axons is high because mitochondrial axonal transport in the retinal explants was rarely observed despite maintaining the retinal explants under the conditions optimized for long-term retinal cultures. Cutting of the optic nerves (RGC axons) to prepare retinal explants induced excessive mitochondrial fragmentation in the RGC axons. Time is indicated as min:s.

Movie S2. Z-stack images of minimally invasive intravital imaging of the mouse retina through the sclera. ONH is on the right side of Movie S2. The movie shows distinct layers in the retina, including the retinal pigment epithelium, deeper layer of the retinal vascular system, inner nuclear layer, inner plexiform layer, RGC cell bodies and dendrites in the ganglion cell layer, and RGC axons in the nerve fiber layer. Individual RGC axons commonly project to ONH. Depth is indicated at the lower left.

Movie S3. Three-dimensional images of minimally invasive intravital imaging of the mouse retina through the sclera from the inner plexiform layer to the nerve fiber layer demonstrate the entire image of RGC (arrowhead in Fig. S3*G*) with subcellular resolution, including the RGC axon and dendrites. ONH is on the right side of Movie S3.

Movie S4. The sheet structure of the nerve fiber layer permits intravital sequential time-lapse imaging of mitochondria transported in a single axon with submicrometer resolution (MIMIR), which shows preserved blood flow (open arrow) and highly dynamic mitochondrial axonal transport (arrowheads, RGC cell bodies; asterisks, RGC axons) in the mammalian CNS in vivo under physiological conditions. The dynamics of mitochondrial axonal transport in MIMIR are clearly different from those in the explant imaging of the retina (Movie S1). Note that in Movie S4 with submicrometer resolution, focus is maintained for 5 min without artifacts caused by heartbeat and breathing. Movie S4, which was acquired every 3 s without *z*-stacks, shows that MIMIR did not cause phototoxicity during 5 min. Time is indicated as min:s.

Movie S5. MIMIR shows that mitochondria are transported from and to the RGC cell body (arrowhead) in the axon (asterisk). Note that the first varicosity (open arrow) from the RGC cell body is apparently larger than the second varicosity. Time is indicated as min:s.

Movie S6. MIMIR shows that characteristically long, snake-like mitochondria are smoothly transported through the curve of the RGC axon (asterisk). The length of the first snake-like mitochondrion is greater than 10 μm. Time is indicated as min:s.

Movie S7. MIMIR of adult control mice (age, 4 months) shows preserved blood flow (open arrow)

and active mitochondrial transport in axons (asterisks). Time is indicated as min:s.

Movie S8. MIMIR of adult mice with experimental glaucoma 3 d after laser treatment shows an axon (asterisk) in which mitochondrial axonal transport decreases and mitochondria-free regions increase, although an axon (double asterisk) with active transport and preserved blood flow (open arrow) are observed. Time is indicated as min:s.

Movie S9. MIMIR can be performed in middle-aged mice (12–13 months) under physiological conditions. MIMIR of middle-aged mice shows active mitochondrial transport in axons (asterisks) with preserved blood flow (open arrow). Time is indicated as min:s.

Movie S10. MIMIR can be conducted in old mice (23–25 months) under physiological conditions. MIMIR (arrowheads, RGC cell bodies) of old mice shows active mitochondrial transport in axons (asterisks) with preserved blood flow (open arrow). Time is indicated as min:s.

Movie S11. MIMIR shows bilateral mitochondrial axonal transport that starts from the upper right side of Movie S11. Time is indicated as min:s.

Movie S12. MIMIR shows continuous mitochondrial axonal transport (asterisk) that starts from the upper left side of Movie S12. Time is indicated as min:s.

Movie S13. MIMIR shows that mitochondrial axonal transport pauses in the region where other mitochondria exist (asterisk), which starts from the left side of Movie S13. Time is indicated as min:s.

Movie S14. MIMIR shows that mitochondrial axonal transport pauses in the mitochondria-free region, which starts from the lower left side of Movie S14. Time is indicated as min:s.

Movie S15. MIMIR in old mice (arrowheads, RGC cell bodies) with experimental glaucoma 3 d after laser treatment shows less mitochondrial axonal transport in the RGC axons (asterisks) than that in adult mice with experimental glaucoma 3 d after laser treatment, although mitochondrial axonal transport (arrow) and preserved blood flow (open arrow) are observed. Time is indicated as min:s.

References for SI

1. Misgeld T, Kerschensteiner M, Bareyre FM, Burgess RW, Lichtman JW (2007) Imaging axonal transport of mitochondria in vivo. *Nat Methods* 4(7):559–561.

2. Johnson TV, Martin KR (2008) Development and characterization of an adult retinal explant organotypic tissue culture system as an in vitro intraocular stem cell transplantation model. *Invest Ophthalmol Vis Sci* 49(8):3503–3512.

3. Imanishi Y, Batten ML, Piston DW, Baehr W, Palczewski K (2004) Noninvasive two-photon imaging reveals retinyl ester storage structures in the eye. *J Cell Biol* 164(3):373–383.

4. Yuki K, Yoshida T, Miyake S, Tsubota K, Ozawa Y (2013) Neuroprotective role of superoxide dismutase 1 in retinal ganglion cells and inner nuclear layer cells against N-methyl-D-aspartate-induced cytotoxicity. *Exp Eye Res* 115:230–238.

5. Reichstein D, Ren L, Filippopoulos T, Mittag T, Danias J (2007) Apoptotic retinal ganglion cell death in the DBA/2 mouse model of glaucoma. *Exp Eye Res* 84(1):13–21.

6. Fu CT, Sretavan DW (2012) Ectopic vesicular glutamate release at the optic nerve head and axon loss in mouse experimental glaucoma. *J Neurosci* 32(45):15859–15876.

7. Yasuda M, Tanaka Y, Ryu M, Tsuda S, Nakazawa T (2014) RNA sequence reveals mouse retinal transcriptome changes early after axonal injury. *PLoS One* 9(3):e93258.

8. Fleige S, Pfaffl MW (2006) RNA integrity and the effect on the real-time qRT-PCR performance. *Mol Aspects Med* 27(2–3):126–139.

9. Ueno S, et al. (2005) Physiological function of S-cone system is not enhanced in rd7 mice. *Exp Eye Res* 81(6):751–758.

10. Vossel KA, et al. (2010) Tau reduction prevents Abeta-induced defects in axonal transport. *Science* 330(6001):198.

11. Gilley J, et al. (2012) Age-dependent axonal transport and locomotor changes and tau hypophosphorylation in a "P301L" tau knockin mouse. *Neurobiol Aging* 33(3):621.e1–621.e15.

12. Magrane J, Cortez C, Gan WB, Manfredi G (2014) Abnormal mitochondrial transport and morphology are common pathological denominators in SOD1 and TDP43 ALS mouse models. *Hum Mol Genet* 23(6):1413–1424.

13. Anderson DR, Hendrickson A (1974) Effect of intraocular pressure on rapid axoplasmic transport in monkey optic nerve. *Invest Ophthalmol* 13(10):771–783.

14. Pease ME, McKinnon SJ, Quigley HA, Kerrigan-Baumrind LA, Zack DJ (2000) Obstructed axonal transport of BDNF and its receptor TrkB in experimental glaucoma. *Invest Ophthalmol Vis Sci* 41(3):764–774.

15. Quigley HA, et al. (2000) Retrograde axonal transport of BDNF in retinal ganglion cells is blocked by acute IOP elevation in rats. *Invest Ophthalmol Vis Sci* 41(11):3460–3466.

16. Weinreb RN, Khaw PT (2004) Primary open-angle glaucoma. *Lancet* 363(9422):1711–1720.

17. Radius RL, Anderson DR (1981) Rapid axonal transport in primate optic nerve. Distribution of pressure-induced interruption. *Arch Ophthalmol* 99(4):650–654.

18. Wang J, et al. (2005) A local mechanism mediates NAD-dependent protection of axon degeneration. *J Cell Biol* 170(3):349–355.

19. Baltan S, et al. (2010) Metabolic vulnerability disposes retinal ganglion cell axons to dysfunction in a model of glaucomatous degeneration. *J Neurosci* 30(16):5644–5652.

20. Ju WK, et al. (2008) Intraocular pressure elevation induces mitochondrial fission and triggers OPA1 release in glaucomatous optic nerve. *Invest Ophthalmol Vis Sci* 49(11):4903–4911.

21. Cho DH, et al. (2009) S-nitrosylation of Drp1 mediates beta-amyloid-related mitochondrial fission and neuronal injury. *Science* 324(5923):102–105.

22. Alexander C, et al. (2000) OPA1, encoding a dynamin-related GTPase, is mutated in autosomal dominant optic atrophy linked to chromosome 3q28. *Nat Genet* 26(2):211–215.

23. Delettre C, et al. (2000) Nuclear gene OPA1, encoding a mitochondrial dynamin-related protein, is mutated in dominant optic atrophy. *Nat Genet* 26(2):207–210.

24. Zuchner S, et al. (2004) Mutations in the mitochondrial GTPase mitofusin 2 cause Charcot–Marie–Tooth neuropathy type 2A. *Nat Genet* 36(5):449–451.

25. O'Connell K, Ohlendieck K (2009) Proteomic DIGE analysis of the mitochondria-enriched fraction from aged rat skeletal muscle. *Proteomics* 9(24):5509–5524.

26. Rana A, Rera M, Walker DW (2013) Parkin overexpression during aging reduces proteotoxicity, alters mitochondrial dynamics, and extends lifespan. *Proc Natl Acad Sci USA* 110(21):8638–8643.